Characterization of an Electron Gun for Hollow Electron Beam Collimation

Siqi Li*

Undergraduate Student at University of Chicago and Fermilab Lee Teng Intern

Giulio Stancari (supervisor)

Fermi National Accelerator Laboratory, P.O. Box 500, Batavia, Illinois 60510, USA

(Dated: August 17, 2012)

Hollow electron beam collimation (HEBC) is a new technique developed to complement conventional beam collimation system to remove beam halo in a controlled fashion. We study the characteristics of the electron gun that produces the hollow electron beam. Cathode yield and beam profile measurements are used to extract information on gun performance. Results of characteristic measurements are presented.

*E-mail: lisiqi@fnal.gov

Contents

I. INTRODUCTION

We are studying hollow electron beams as a new collimation technique for high-intensity beams in storage rings and colliders. A detailed introduction can be found at Ref. [1].

The collimation system is important in high-energy particle accelerators and storage rings, because it protects equipment from damage due to particle aborts. It is also used for controlling and reducing the beam halo, which is continuously produced by processes such as beam-gas scattering, intrabeam scattering, electrical noise in the accelerating cavities, ground motion, betatron resonances, and beam-beam collisions. Beam halo is undesirable because it is a potential cause for unwanted radioactivity and a source of experimental backgrounds. Therefore, it is of great interest to develop an effective collimation technique that removes the beam halo.

Conventional collimation system (Figure 1) consists mainly of two-stage collimators, possibly followed by successive stages. They include primary collimators (the targets) and secondary collimators (the absorbers). The primary collimator is the device that is closest to beam core and generates random transverse kicks via multiple Coulomb scattering. For example, in the Tevatron, the primary collimators are 5-mm tungsten plates placed about 5 standard deviations (σ) away from the beam core. The random multiple-scattering kick has a root mean square of 17 μrad for 980-GeV protons. The secondary collimator is placed farther away from the beam core than the primary. The affected particles from the primary stage, as well as the newly-produced particles from the primary collimator, get absorbed by the secondary collimator. In the Tevatron, the secondary collimators are 1.5-m steel blocks placed at 6σ away from the beam core. If necessary, more collimators are placed following the secondary collimator to increase the absorption efficiency.

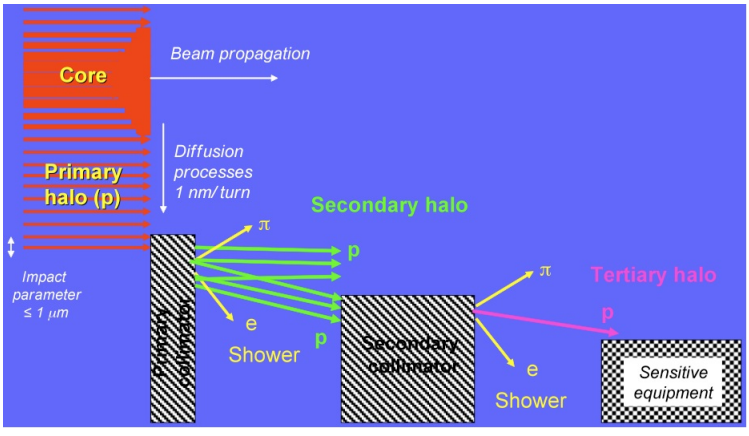

FIG. 1: Mechanism of conventional collimator system (picture courtesy of R. Assmann). The picture shows the circulating beam and the first two stages of the collimation system.

The conventional two-stage collimation system effectively shields sensitive equipment from beam aborts, and reduces beam-related background in experiments. However, it has two main limitations. First, in a high-energy particle accelerator, no material can be placed too close to the beam. Placing the collimator too close to the beam results in increased beam loss rates and radiation damage. The electromagnetic impedance of the collimator also gives some constraints on collimator placement. Another problem is beam jitter. The beam oscillates as a result of mechanical vibrations, such as ground motion. Even with active orbit stabilization, the beam centroid may oscillate by tens of microns. This translates into periodic bursts of losses at aperture restrictions.

To address these limitations, magnetically confined hollow electron beams are being studied as a new collimation technique. In a hollow electron beam collimator (HEBC), electrons enclose the circulating beam immersed in a solenoidal field. (Figure 2). The electron beam is generated by a pulsed electron gun, and it is transported with strong axial magnetic fields, in an arrangement similar to electron cooling and electron lenses. Because of its low impedance, we can place the HEBC very close to the circulating beam and even overlap with it, without leading to any material damage. In addition, the HEBC reduces the beam sensitivity to surrounding vibration.

The electric charge of the electrons kicks halo particles transversely according to the following equation:

$$\theta = \frac{2I_r L(1 \pm \beta_e \beta_p)}{r\beta_e \beta_p c^2 (B\rho)_p} \left(\frac{1}{4\pi\varepsilon_0}\right), \tag{1}$$

where I_r is the beam current, L is the length of the overlap region, $B\rho$ is the proton beam rigidity, ε_0 is the vacuum permittivity, $\beta_e c$ is the electron velocity, and $\beta_p c$ is the particle velocity. The + sign indicates that

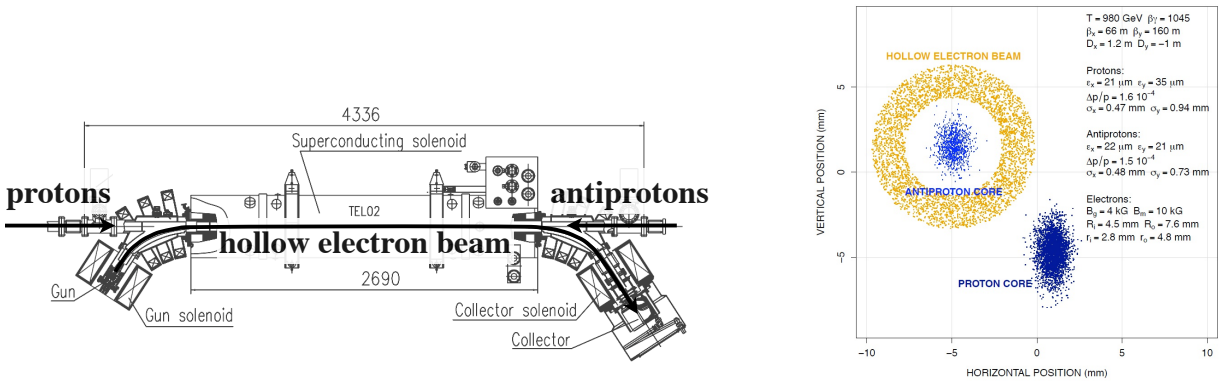

FIG. 2: Left: experimental layout of a Tevatron Electron Lens (TEL-2). The experimental apparatus consists of three solenoids, namely the gun solenoid where the gun is installed, the main solenoid, where HEBC acts on circulating beams, and collector solenoid, where electrons are collected. Right: cross section of HEBC acting on antiproton beam. The HEBC surrounds the circulating beam and kicks halo particles away from the beam core.

the magnetic force and electric force are in the same direction. For typical parameters, the kick given to a 980-GeV proton is on the order of 0.2 μrad.

Several measurements have been done in Fermilab's Tevatron to test the compatibility of the HEBC with collider operations, acting on the antiproton beam (Figure 2). The effects of the HEBC on antiproton beam include scraping the beam halo while leaving the beam core unperturbed, increasing halo diffusion rate, and removing the correlation between beam losses from different bunch trains and hence reducing sensitivity to beam jitter. A detailed description and data analysis of such studies can be found in Refs. [2] and [4].

This project focused on characterizing a new 1-inch-diameter hollow electron gun, for possible use at CERN in the LHC or SPS machine. The major goal of this project is to test the feasibility of a larger and more powerful gun than that tested at Fermilab's Tevatron. The cathode yield as a function of voltage and temperature and the electron beam profile are of particular interest. They provide a tool for diagnosing the performance of the cathode and understanding its geometry and operation, so that we have a better control over the produced pulsed electrons. In addition, we analyzed our data according to a model describing the transition between current densities in different regimes, which is important in diagnosing the surface uniformity of the emitter. In this paper, we present the characteristics of the hollow electron beam measured at the Fermilab Electron Lens Test Stand.

II. PRINCIPLES OF THERMIONIC ELECTRON GUNS

We used a thermionic dispenser cathode as our source of electrons. A thermionic dispenser cathode is a device that emits electrons according to thermionic emission mechanism. As one increases the temperature of cathode surface, electrons in the cathode can escape from the surface of the cathode when the energy gained from heating reaches a certain value. The threshold energy above which electrons are thermally excited to escape the cathode is the sum of Fermi level energy and work function, $E_0 + e\phi$. The work function is determined by the cathode material.

Using the Fermi-Dirac distribution and appropriate approximations, one can derive the Richardson-Dushman equation to describe the relation between emission current density and temperature of a cathode with no applied electric field:

$$J = A_0 T^2 e^{-\frac{e\phi}{kT}}, \tag{2}$$

where A_0 is a universal constant and has a value 1.20×10^6 A/m^{2}K^2. A detailed derivation can be found in Ref. [3]. The anode is set to a higher electric potential with respect to the cathode. The presence of the anode creates an electric field, whose effect is not considered in the Richardson-Dushman equation. To include the

effect of the applied electric field on an emitted electron, one can consider the increase in its kinetic energy as the electron moves in between the cathode and the anode. The increase in kinetic energy is the same as the corresponding decrease in potential energy. In addition to the applied field, the emitted electron induces an image charge in the cathode, which creates a surface field via the Coulomb force between the emitted electron and the image charge. Therefore the total electric field experienced by the emitted electron is the sum of the applied field and the surface field. The effect of the applied field is called the Schottky effect. Taking the Schottky effect into account, we can correct the Richardson-Dushman equation as follows,

$$J = A_0 T^2 e^{-\frac{e}{kT}[\phi - \sqrt{\frac{eE_a}{4\pi\varepsilon_0}}]}, \tag{3}$$

where E_a is the electric field strength between the cathode and the anode.

The above analysis addresses the relation between emission current density and temperature. This regime is called temperature limited (TL) regime. However, as the voltage increases, the cathode will reach its full space-charge limit (FSCL) regime, where increasing temperature does not affect the emission current. The space-charge effect is a result of the negative charge of electrons, which reduces the potential energy at the surface of the cathode. This limit occurs when the density of electrons adjacent to the cathode surface becomes so large that the potential energy reduces below zero and the electrons are forced to flow back to the cathode. In this regime, one can study the relation between emission current in relation to cathode-anode voltage. Applying energy conservation law and Poisson's equation, one can get the relation between emission current and voltage as follows,

$$I = PV^{\frac{3}{2}}, \tag{4}$$

where P is known as the perveance of the diode. This is called the Child-Langmuir law. Perveance is a function only of the geometry of the diode, and therefore it is a useful tool in diagnosing the cathode geometry, which is addressed below in Section IV.

Note that the previous discussion on perveance does not take the electrons' relativistic effect into account. When the electrons get accelerated to a very high velocity, their motion can be described in the relativistic regime. Reiser [8] discusses a generalized perveance which accounts for the relativistic effect. The relation between the cathode yield current and cathode-anode voltage can be described by the following equation,

$$I = \frac{I_0}{2(1-\gamma^2 f_e)} K(\beta\gamma)^3, \tag{5}$$

where I_0 is a constant, γ and β are the Lorentzian factors in special relativity, K is the generalized perveance, and f_e is the neutralization factor for electrons. I will discuss each term below. I_0 is a constant defined as

$$I_0 = \frac{4\pi\varepsilon_0 m_e c^3}{e} = 17 \text{ kA}, \tag{6}$$

where ε_0 is the vacuum permittivity, m_e is the electron mass, and c is the speed of light. The Lorentzian factors γ and β can be calculated from the cathode-anode voltage and electron's rest mass. The generalized perveance, K, is a dimensionless value. The neutralization factor f_e describes the fraction of electrons neutralized by the rest gas in the vacuum chamber, and it is expected to be between 0 and 1. Because of the energy dependence of the ionization cross section, neutralization is more likely to occur at low voltages. By comparing the shape of perveance and generalized perveance as a function of voltage, one can tell whether the transition into temperature limited regime or the relativistic effect is more important. A more detailed analysis can be found at Section IV.

To describe the transition of the emission curve from one regime to the other, Longo proposed the following model [5],

$$\frac{1}{J} = \frac{1}{J_{sc}} + \frac{1}{J_{tl}}, \tag{7}$$

where J is the observed current density, J_{sc} is the theoretical current density in space-charge limited regime, and J_{tl} is the theoretical current density in temperature-limited regime. In Longo's paper, he discusses the change of the emission curve shape as the cathode ages. He adopts Vaughan's suggestion [6] to raise each term of Equation 7 to a power α, known as the shape factor. The modified equation is

$$\frac{1}{J^\alpha} = \frac{1}{J_{sc}^\alpha} + \frac{1}{J_{tl}^\alpha}. \tag{8}$$

The parameter α is related to the uniformity of the emitter surface. It has been generally accepted that the more uniform the emitter surface is, the sharper the transition of the emission curve is. Figure 3 illustrates how the change in the shape factor α changes the transition of the emission curve.

III. ELECTRON LENS TEST STAND

The electron lens test stand is located in Fermilab's lower linac gallery (Figure 4). It was originally developed for the Tevatron electron lenses, but now it is also used for testing hollow electron guns. The main experimental apparatus consists of a pulsed electron gun, a straight beamline, and a collector. The vacuum beam line is surrounded by three solenoids. Figure 4 (top) is a photograph of the main apparatus. The three solenoids are called, from left to right in Figure 4, the gun solenoid, the main solenoid, and the collector solenoid.

The gun solenoid surrounds the electron gun. For a typical magnetic strength of 0.3 T, the current in the coil in the gun solenoid is approximately 1800 A. The main solenoid needs four times the current in the coil to provide a 0.3 T magnetic field. The 3-m straight beamline is equipped with pickup electrodes

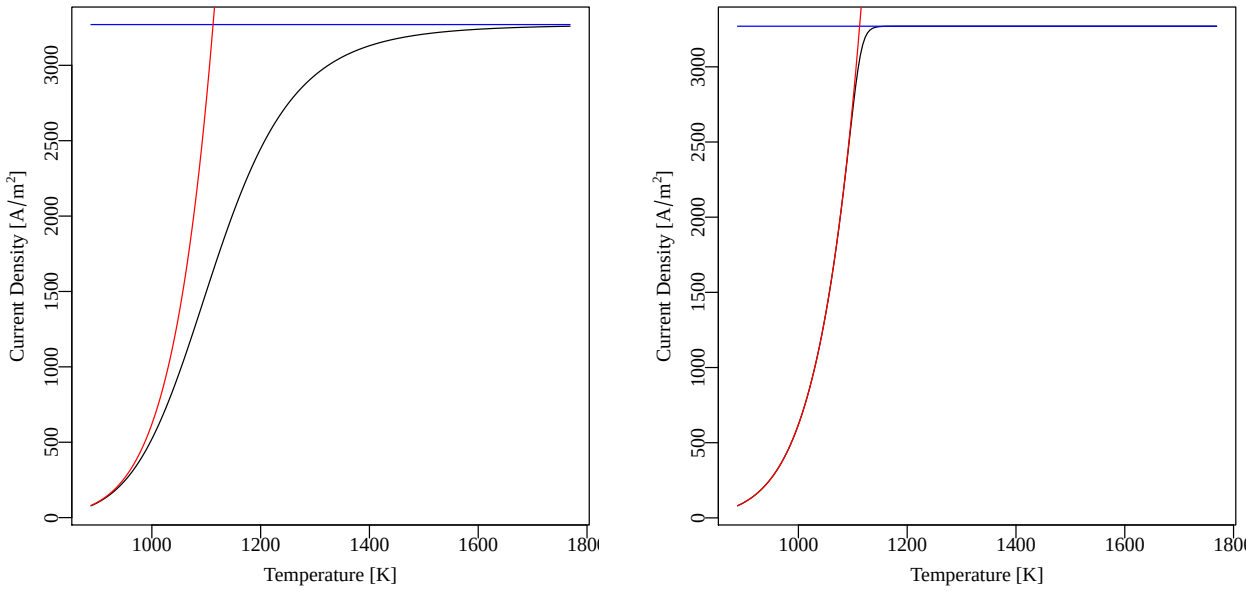

FIG. 3: Example of the effect of the shape factor on the transition between the temperature-limited and the space-charge limited regimes. Cathode-anode voltage at 7000 V, shape factor α=1 (left) and shape factor α=10. The curves represent the current densities, J (black), J_{sc} (blue), J_{tl} (red).

and corrector coils. The electron collector is installed in the collector solenoid. The current in the collector solenoid runs at 1800 A to provide a 0.3 T magnetic field. The collector has a 0.2-mm-diameter pinhole for current-density profile measurements, which are detailed below. This configuration is usually referred to as a "3-3-3 kG configuration". An 18-MΩ low-conductivity cooling water circuit provides cooling for the power supplies, solenoids, and the collector.

The vacuum environment in the beamline is provided by two pumping systems. The primary one is used for fore vacuum (10^{-6} mbar), and it is based on a turbo molecular pump by a diaphragm pump. The secondary one is used to reach high vacuum (10^{-8} mbar), and it consists of three ion pumps.

To characterize the electron gun, we mainly studied the cathode yield and beam profile. The cathode yield describes the yield current as a function of the cathode-anode voltage and as a function of cathode temperature. Electrons are produced in pulses from the electron gun. The pulse width and period are monitored by an oscilloscope. Different settings of the pulse width and pulse period allow us to achieve different voltages and peak currents, keeping the average current approximately constant. The beam current was read out from the output of the collector. The output current goes through two toroids, which measure the voltage across each toroid. The output is displayed on an oscilloscope as a voltage pulse. The voltage is measured as the average amplitude voltage of the pulse. This voltage is calibrated against current such that 1 V corresponds to 1 A collector current.

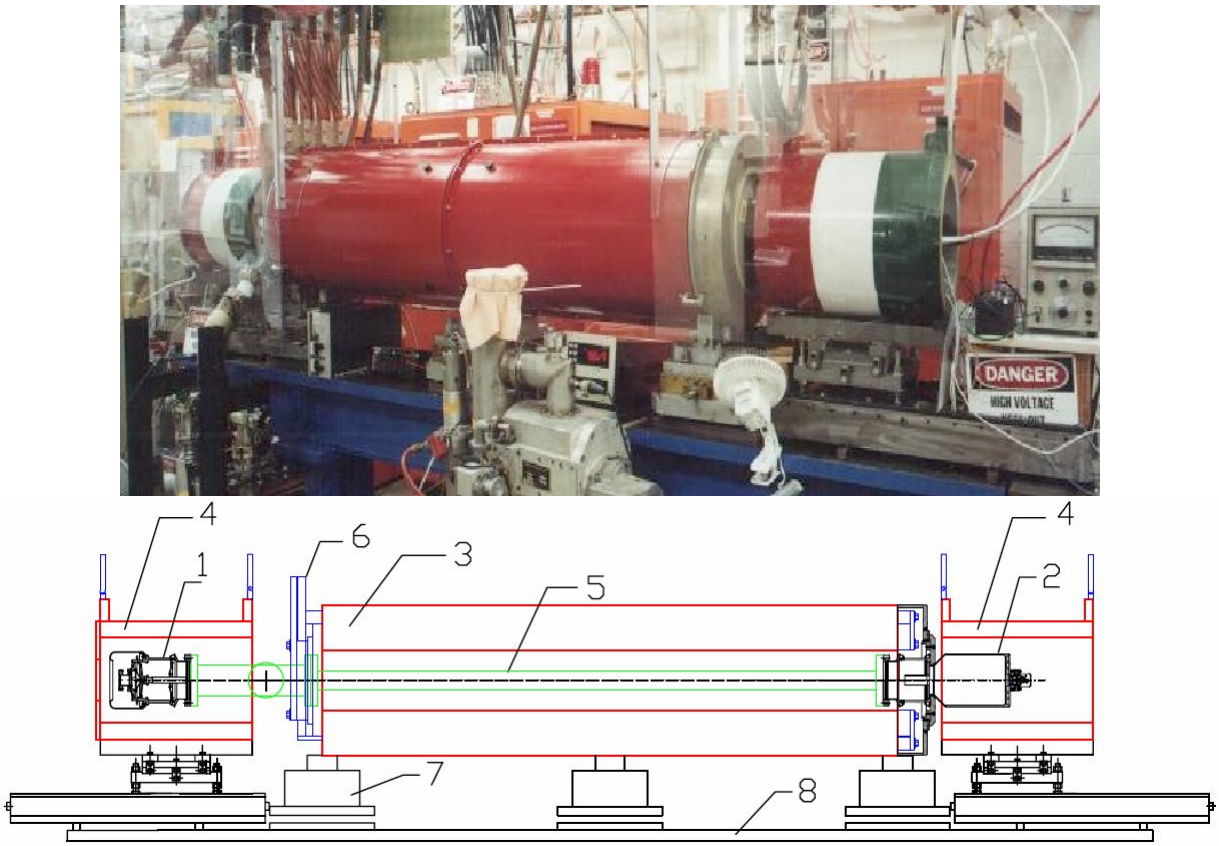

FIG. 4: Electron lens test stand at Fermilab lower linac gallery. The main experimental apparatus consists of a pulsed electron gun, a straight beamline, and a collector. There are three solenoids: gun solenoid (left), main solenoid (middle), and collector solenoid (right). Note that the main solenoid in the middle for testing electron guns is not superconducting as in Figure 2.

The current density profile is measured by recording the current through the collector pin hole while sweeping the electron beam with the magnetic correctors in small steps. A software has been developed to monitor the run throughout the measurement. Examples of profile measurements are given in Section IV below.

IV. 1-INCH HOLLOW ELECTRON GUN

A. Main Features

A high-perveance gun was developed to generate the hollow electron beam. A tungsten dispenser cathode with BaO:CaO:Al_2O_3 impregnant is used to obtain high perveance and appropriate work function (Ref. [3]). Theoretically, the tungsten melting point is 3410 °C, and the work function is 4.6 eV. For barium, the melting point is 725 °C, and the work function is 2.7 eV. When the cathode is heated for a long

enough time, typically after a few hours, the barium diffuses into the pores on the tungsten surface, and hence decreases the effective work function to 1 to 2 eV.

B. Design Considerations

To approximately determine the required size of the hollow electron gun, we considered typical LHC parameters. The energy of the proton beam is 7 TeV, corresponding to a Lorentzian γ_r approximately 7×10^3. The beam size is calculated using the transverse amplitude function, which is approximately $\beta = 200$ m, and the transverse normalized emittance, which is approximately $\varepsilon = 2$ μm. The transverse root-mean-square beam size is therefore

$$\sigma = \sqrt{\frac{\beta\varepsilon}{\gamma_r}} = \sqrt{\frac{(200 \text{ m}) \cdot (2 \times 10^{-6} \text{ m})}{(7 \times 10^3}}) = 0.24 \text{ mm}. \tag{9}$$

Assuming the beam follows a Gaussian distribution transversely, the beam core is within $3\sigma = 0.72$ mm. The inner radius of the hollow electron beam should span approximately 4σ to 8σ, corresponding to 0.96 mm to 1.92 mm. The above dimension applies to the main superconducting solenoid, where the magnetic field strength should be larger than 1 T for stability and smaller than 6 T due to technological limitations. Similarly, in the conventional gun solenoid, the appropriate magnetic field strength should be larger than 0.2 T and smaller than 0.4 T. The flux of the magnetic field remains approximately constant in the transition between the gun and main solenoids. Therefore, the radius of beam in the gun solenoid, r_{gun}, and the radius of beam in the main solenoid, r_{main}, follow this relation:

$$r_{gun} = r_{main}\sqrt{\frac{B_{main}}{B_{gun}}}, \tag{10}$$

where B_{gun} and B_{main} are the respective magnetic field strength in the gun and main solenoids. Because $1.58 < \sqrt{\frac{B_{main}}{B_{gun}}} < 5.48$, we chose the inner radius of the hollow electron beam $r_{gun} \approx 7$ mm.

We have neglected the effect of dispersion D due to the beam momentum spread $\Delta p/p$. If we were to take dispersion into account, the beam size would be $x^2 = (D\Delta p/p)^2 + \sigma^2$. For the LHC, we consider the hollow electron beam dispersion $D \approx 1$ m, and the momentum spread $\Delta p/p \approx 1.5 \times 10^{-4}$. So, $x^2 = 10^{-8}$ m$^2 + 10^{-5}$ m^2, and we can see that the first term is negligible.

Figure 5 shows the longitudinal cross section of the 1-inch hollow electron gun. The outer diameter of the cathode is 25.4 mm (1 in). The diameter of the hole is 13.5 mm, consistent with our calculation using LHC parameters. The electrodes around the cathode help focus the electron beam. Figure 6 (top) is a photograph of the cathode, which is the tungsten hollow cylinder in the middle. Figure 6 (bottom) is a photograph of the entire gun, with cathode, anode and electrodes assembled together.

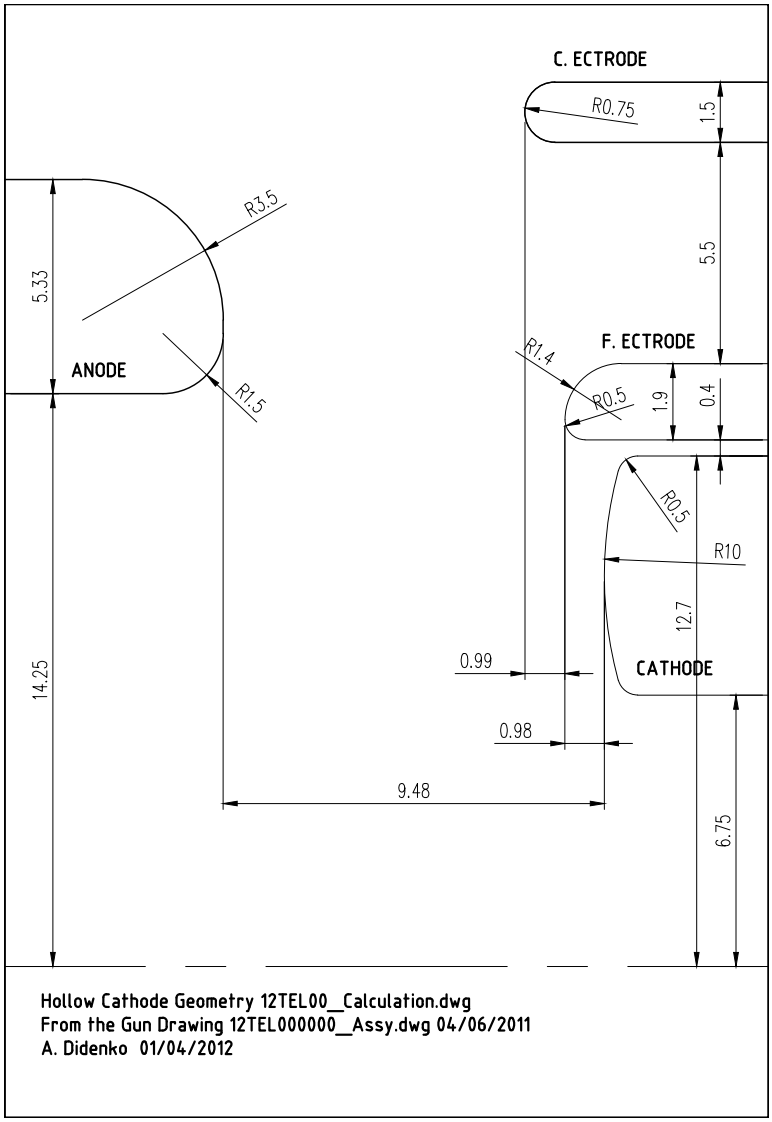

FIG. 5: 1-Inch Hollow Gun Dimensions.

C. Perveance Measurement

The perveance, as introduced above, relates the gun yield current to the cathode-anode voltage. We measured the perveance over a large range of temperatures and voltages. Figure 7 shows an example of the pulse shape on an oscilloscope. The purple curve shows the pulse of the voltage modulator, and the green curve shows the pulse measured by the toroid at the collector. We took the amplitude of the green curve as the peak yield current.

We have taken two sets of data to study cathode perveance. One was taken from December, 2011 to

FIG. 6: Photographs of the 1-inch hollow electron gun. Top: detail of the cathode. Bottom: assembled gun.

FIG. 7: Example of pulse shape shown on an oscilloscope for perveance measurement: modulator voltage (purple trace) and collector current (green trace).

February, 2012. The other was taken in June, 2012. Figure 8 compares the two data sets. Data points were taken when the heating filament current equals 8.75 A, corresponding to a cathode temperature of approximately 1100 °C. The uncertainty in current was calculated by adding a constant uncertainty of 0.05 mA in reading from the oscilloscope, an estimate of measurement uncertainty of 0.1%, and a systematic uncertainty of 1 mA from difference between toroids that measure the collector current in quadrature. The uncertainty in voltage is negligible. The least square fit is weighted by the square of uncertainty reciprocals. The earlier data set shows a perveance of $(4.13 \pm 0.01) \times 10^{-6}$ A/V$^{\frac{3}{2}}$, and the more recent one shows a perveance of $(4.15 \pm 0.02) \times 10^{-6}$ A/V$^{\frac{3}{2}}$. These two values of perveance from two data sets taken at different times are consistent within uncertainty. The blue curves in Figure 8 represent the results of SAM simulation [7]. It can be seen that our measurements are systematically lower than simulation, and this discrepancy is currently not understood and being investigated.

Both data sets show the fitted curve above the data points for higher voltages. We can interpret this by considering two aspects. One is that the uncertainty includes a term proportional to the voltage, and since the weight is the square of uncertainty reciprocal, the fitting is weighted more towards lower voltage than higher voltage. Moreover, the deviation of the fit from the measurements at higher voltage tells us that as we increased voltage, we were pushing towards the temperature limited regime, where increasing voltage does not have an effect on cathode yield current. In this region, we can see that the power relation between current and voltage tends to level up. This can be further demonstrated by the residual plots in the bottom. In both residual plots, we can see a systematic trend that the residual becomes negative at a certain voltage, and then continues to become more negative as voltage increases.

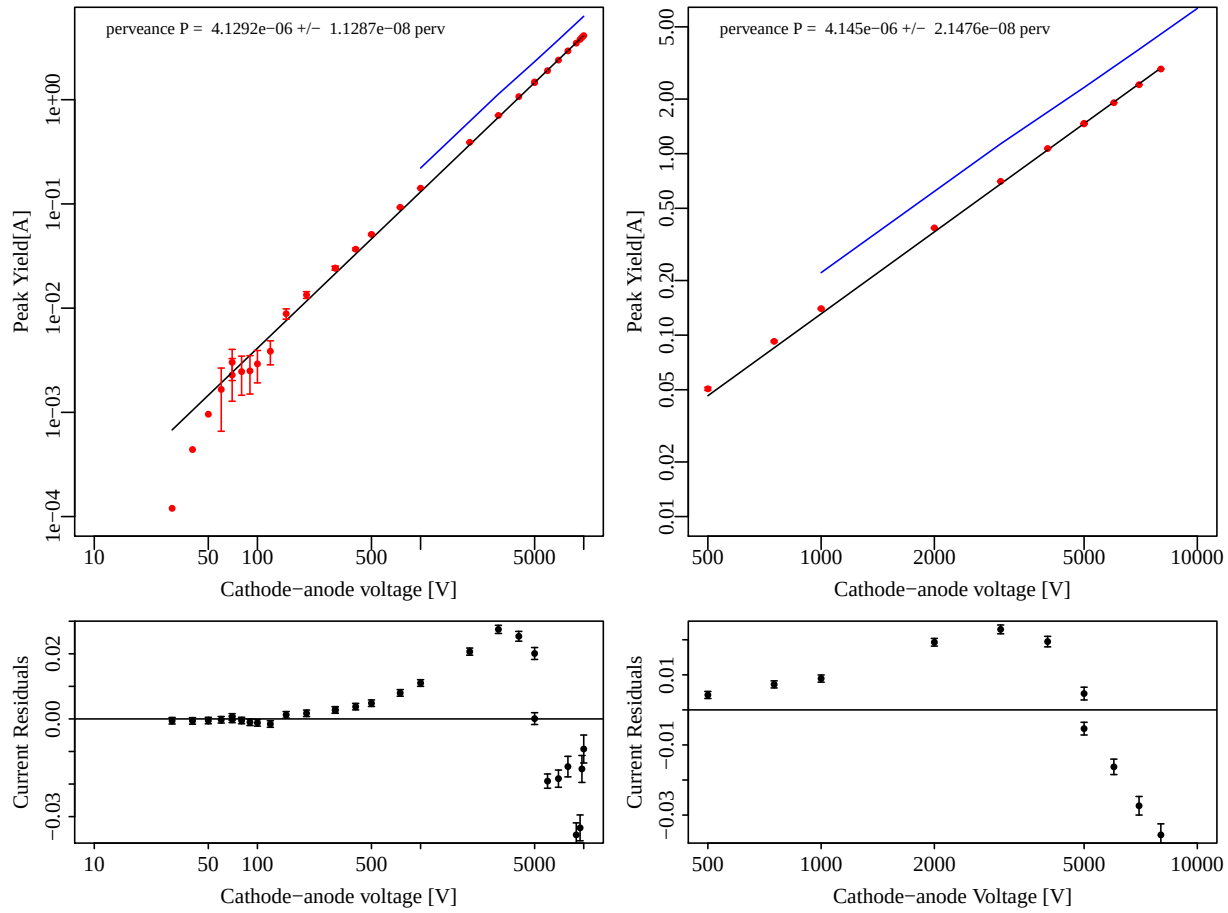

FIG. 8: Perveance analysis using data from December, 2011 - February, 2012 (left), and June, 2012 (right). Top are perveance measurements in logarithmic scale. The blue curves indicate the SAM simulation. Below are residuals.

The relativistic and neutralization effects can be studied using the generalized perveance. With some algebraic manipulation on Eq. 5 and Eq. 6, we can get

$$\frac{K}{1-\gamma^2 f_e} = \frac{2I}{I_0(\beta\gamma)^3}. \tag{11}$$

Let's denote the left-hand-side of Eq. 11 as *LHS*, and plot the right-hand-side as a function of cathode-anode voltage. In Figure 9, we can see that the shape of the perveance and the LHS of Eq. 11 follow a similar trend that as voltage increases, the value tends to decrease slightly and then stay approximately constant. We can extract the value for generalized perveance K from the middle plot at high voltages, because at high voltage, the neutralization fraction f_e is approximately zero. Then we are able to calculate f_e as a function of voltage, as shown in the right plot in Figure 9. The maximum f_e occurs at 70 V, and reaches 20.6%. The fraction f_e decreases as voltage increases, because the higher the energy of the electrons, the less likely they are to ionize with rest gas molecules in the vacuum and get neutralized.

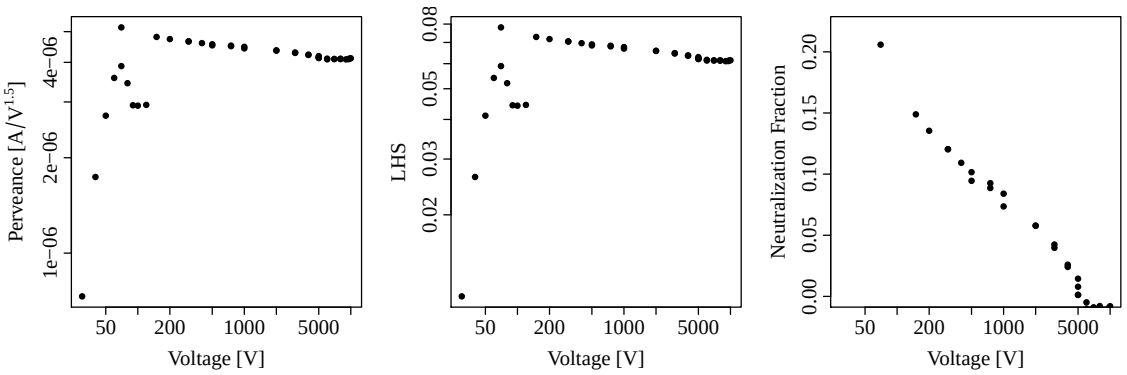

FIG. 9: Generalized perveance analysis. Left: perveance vs. voltage. Middle: left-hand-side of Eq. 11 vs. voltage. Right: neutralization fraction vs. voltage.

TABLE I: Fitting results of Longo's model

Free parameter	1st Quartile	Median	3rd Quartile	Units
α	0.82	0.94	1.07	
P	4.166	4.176	4.187	10^{-6} A/V$^{\frac{3}{2}}$
A_0	5.8	24.6	86.8	10^3 A/m^{2}K^2

D. Cathode Yield vs. Temperature

To study the relation between cathode yield current and temperature, we first calibrated temperature against the resistance of the heating filament.

Figure 10 shows the procedures of our temperature calibration. First (Figure 10 top left), we observed how the filament resistance increased with filament current. Secondly, we studied the relation between peak yield current and filament resistance (Figure 10 top right). The vertical line indicates what we took the temperature to be 1100 °C, corresponding to a filament current of 8.75 A, and a filament resistance of 1.04 Ω. When the filament is at room temperature 300 K, we measured its voltage and current to get its resistance, 0.43 Ω. Assuming a linear relation between temperature and filament resistance, $T = \beta R + T_0$, we can extract the values for β and T_0. We found $\beta = 1765.7$ K/Ω and $T_0 = -462.29$ °C, and Figure 10 lower left illustrates this relation. We leave 50 °C uncertainty in our choice of operating temperature, giving rise to a range for β and T_0, where 1683.47 K/Ω $< \beta <$ 1847.87 K/Ω and -497.78 K $< T_0 < -462.80$ K.

As mentioned in Section II, Longo proposed a model to describe the transition between the space-charge limited regime and the temperature limited regime. Bearing this in mind, we attempted to compare our data with Longo's model to extract some of the physical parameters. Eq. 8 can be written as follows:

$$I_{op} = a[(\frac{1}{J_{sc}})^{\alpha} + (\frac{1}{J_{tl}})^{\alpha}]^{-\frac{1}{\alpha}}, \tag{12}$$

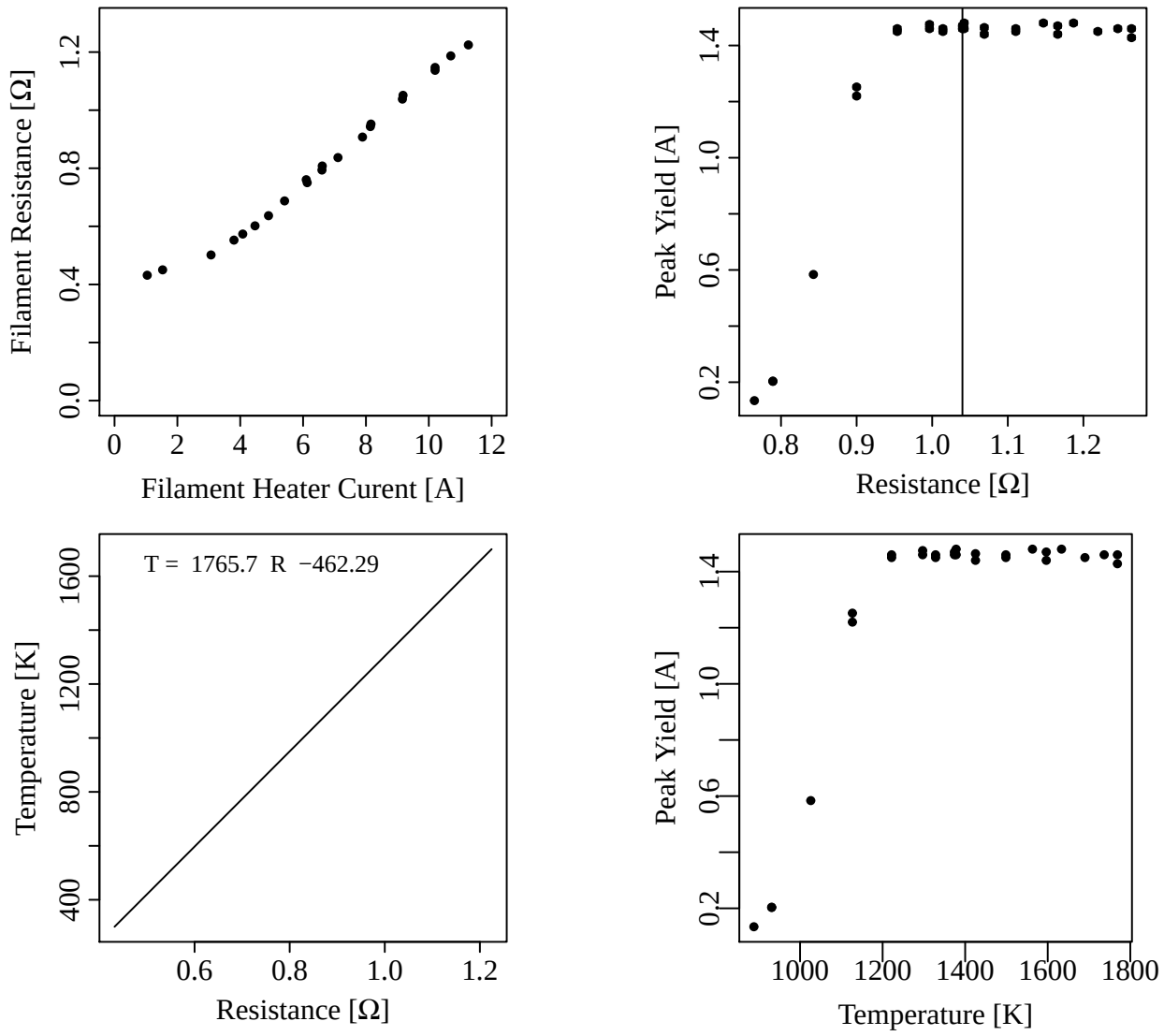

FIG. 10: Temperature calibration using filament resistance. Top left: filament resistance increases with filament current. Top right: peak yield current as a function of temperature. Vertical line indicates the point chosen to correspond to 1100 °C. Lower left: temperature calibration with filament resistance, assuming a linear relation. Lower right: peak yield current as a function of temperature.

where I_{op} is the measured current, a is the effective cathode area, and J_{sc}, and J_{tl} are described by Eq. 4 and Eq. 2, repeated here:

$$J_{sc} = \frac{PV^{\frac{3}{2}}}{a}, \tag{13}$$

$$J_{tl} = A_0 T^2 e^{-\frac{e}{kT}\left[\phi - \sqrt{\frac{eV}{4\pi\varepsilon_0 d}}\right]}, \tag{14}$$

where ϕ is the work function of the cathode surface, and d is the effective distance between the cathode and

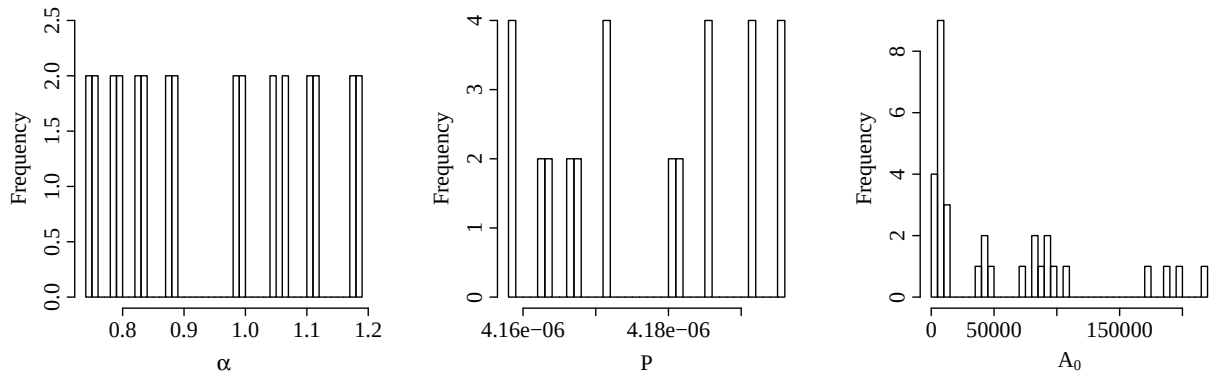

FIG. 11: Histograms of the fitting values for α, P, and A_0.

the anode. Together with the temperature calibration parameters, there are a total of 8 correlated parameters, a, α, d, A_0, P, ϕ, β and T_0. We aim to test whether the measurements can yield reasonable values for these parameters, but do not expect to extract exact values for them. In order to do this, we chose α, P, and A_0 to be free parameters, and set the other parameters within a reasonable range. This choice was made considering our knowledge of these parameters. Work function ϕ depends on the material of the cathode, and is expected to be $1.4\ \text{eV} < \phi < 1.45\ \text{eV}$. Cathode area a and cathode-anode distance d can be found from Figure 5, yielding $a = 3.64 \times 10^{-4}\ \text{m}^2$ and $d = 1 \times 10^{-2}\ \text{m}$. Due to the electrode effects and the concave surface of the cathode, we expect $3.6\ \text{cm}^2 < a < 4\ \text{cm}^2$ and $0.9\ \text{cm} < d < 1.7\ \text{cm}$. The range for β and T_0 are repeated here: $1683.47\ \text{K}/\Omega < \beta < 1847.87\ \text{K}/\Omega$ and $-497.78\ \text{K} < T_0 < -462.80\ \text{K}$. We looped through the different values for these parameters and executed 32 fits, yielding 32 values for each of the free parameters, α, P, and A_0. We expect α to be approximately one, as the case for typical cathodes. As shown in Section IV C, we expect perveance P to be on the order of $4 \times 10^{-6}\ \text{A}/\text{V}^{\frac{3}{2}}$. We do not have an expectation for A_0, as it is a function of the material and gun geometry. Figure 11 shows the histograms for the three free parameters. The α and P histograms are flat, and the A_0 histogram has a long tail, so Gaussian distribution is not a good representation of the data. We chose to use the quartiles to estimate the range of those parameters. Table I shows the results.

Figure 12 illustrates the fitting. The curves represent the fitted model corresponding to different voltages, and the points represent measurements. As we increase the voltage, we see more significant deviation of the model from the measurements. Since the fitting was done with weights equal to the reciprocal of uncertainty squared, we suspect this deviation comes from an overestimation of the proportional term or an underestimation of the constant term in the uncertainty calculation (Section IV C). Also, more discrepancy can be seen at the lower temperature end for high voltage data. Figure 13 plots the histogram of the fitting residuals. The median is 0.66 mA, and the median absolute deviation is 5.5 mA. In general, our measure-

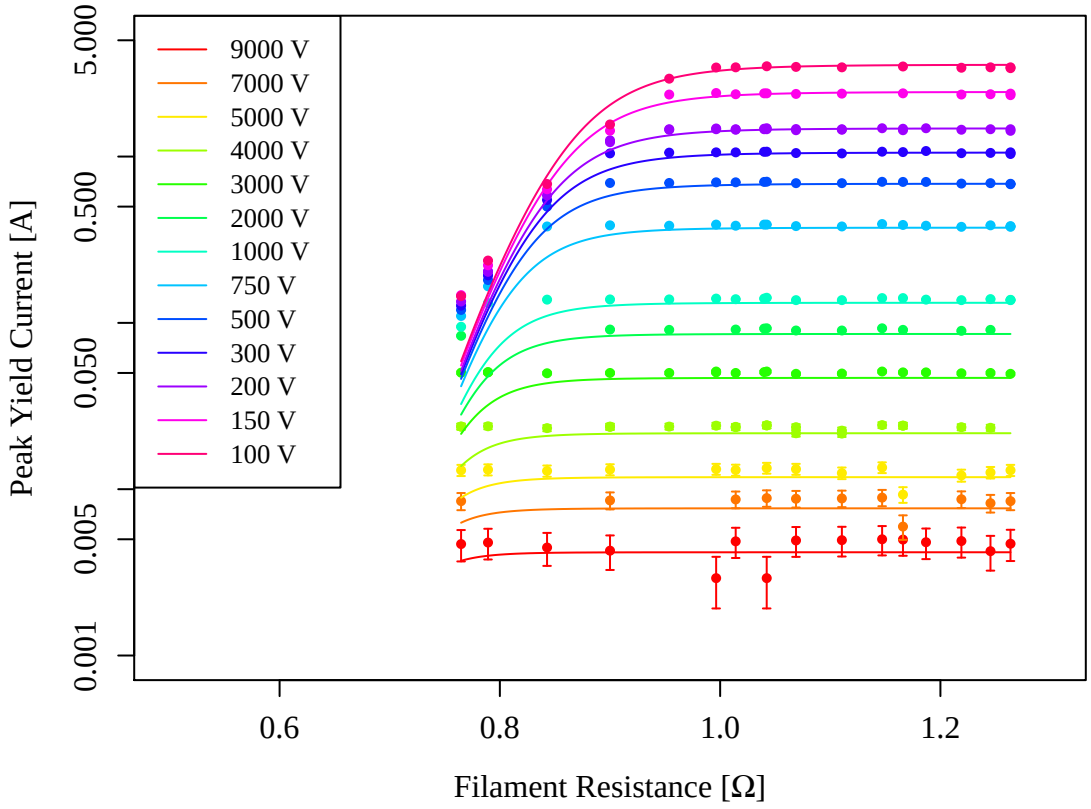

FIG. 12: Comparison of gun yields with Longo's model.

ments are reasonably compatible with Longo's model, and we get reasonable results for the parameters that characterize the hollow electron gun.

E. Beam Profile Measurements

Hollow electron beam profiles were measured at different voltages. Figure 14 compares the 2 dimensional cross section of the hollow electron beam taken at different times and different filament currents. We can see that, horizontally, the current density is stronger in the positive direction than that in the negative direction in all three plots. The asymmetrical pattern can be explained by either an off-axis cathode with respect to the extraction electrode, or an asymmetrical distribution of the solenoid magnetic field. For the latter possibility, we would expect to see different level of asymmetry at different currents. However, we have repeated the profile measurement at different currents, and the profiles show the same asymmetry. Top figure was taken in January 2012, with a filament current at 8.75 A. Middle figure was taken in June 2012,

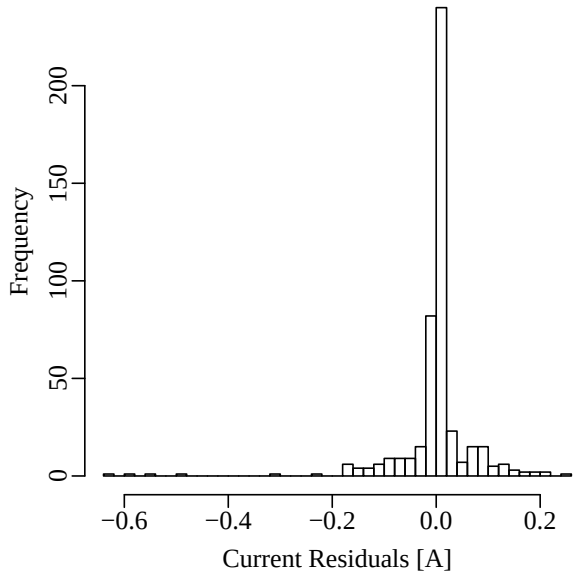

FIG. 13: Residuals of Longo's model fitting.

with a filament current at 8.75 A. In both cases, the peak electron current was 2.9 A. Bottom figure was taken in February 2012, with a filament current at 6.25 A, and a peak current of 0.14 A. If asymmetrical magnetic field is the cause of the asymmetrical beam profile, we would expect the space-charge effect to be more significant in the higher current case. However, we do not see significant difference between the bottom figure and the other two, indicating the asymmetrical pattern comes from the asymmetrical geometry of the gun, instead of the magnetic field. Thus we have identified the cathode to be off-centered with respect to the electrodes. The tolerance on concentricity becomes harder to achieve as we use larger and longer cathode. This 1-inch hollow electron gun is the largest and longest cathode we have used so far.

After we have diagnosed the asymmetry of the cathode with respect to the electrodes, we took out the electron gun from the Electron Lens Test Stand and disassembled it. We measured the average distance between the cathode and the electrode to be (0.4 ± 0.2) mm. The concentricity was improved to (0.40 ± 0.07) mm. The gun was then sent to Fermilab Mechanical Support Department for cleaning and vacuum testing.

In addition to the asymmetrical pattern, we can see a "quadrupole effect" from the 2-dimensional beam profile scan: there is significant current density increase at four points around the circumference of the beam cross section, with the left one lower than the other three due to the asymmetrical pattern in current density. We suspected that this quadrupole effect is due to the four legs supporting the anode (Figure 6). Because of the gap between cathode and anode, emitted electrons can experience the effect of the potential of the four supporting legs, leading to the quadrupole-shaped beam profile. We did not see this effect in

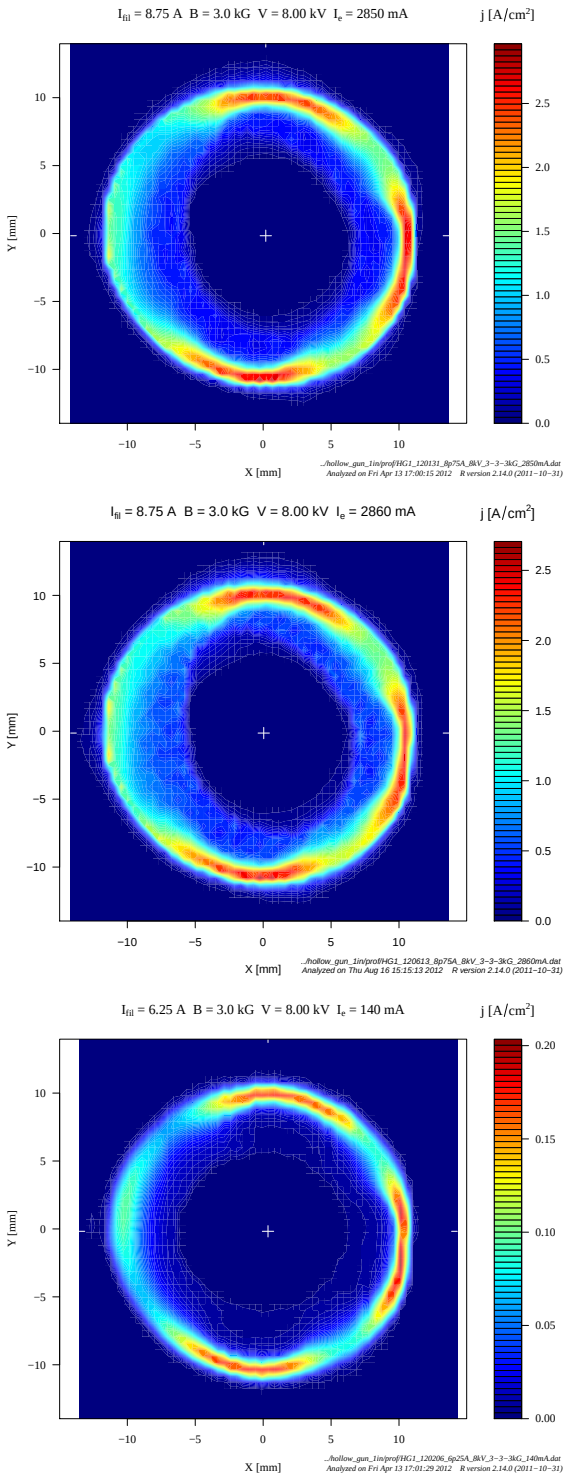

FIG. 14: 2D scan of hollow electron beam taken at 8 kV. High current (top: January, 2012; middle: June, 2012), and low current (bottom: February 2012).

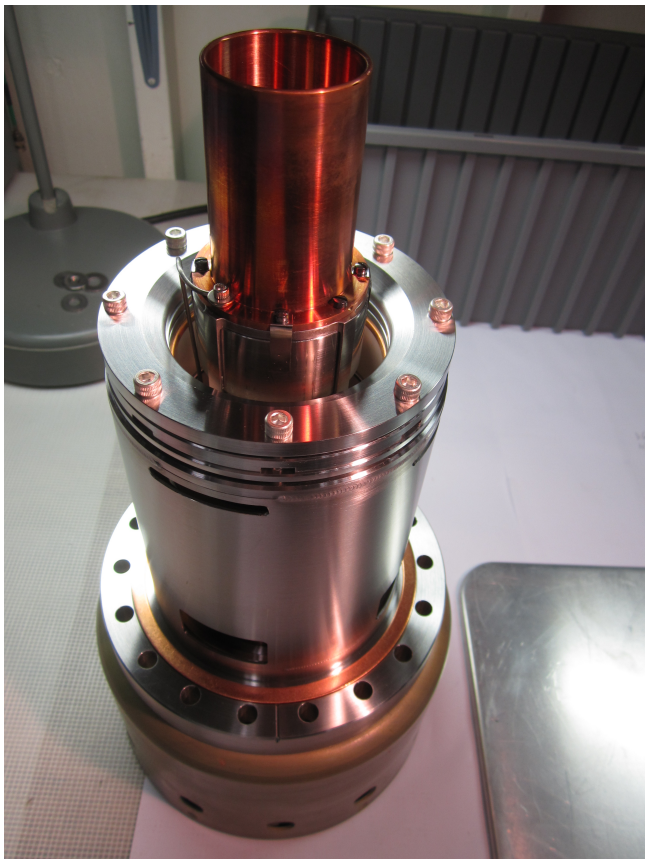

FIG. 15: Modified 1-inch hollow electron gun with added anode shield.

the previous 0.6-inch hollow electron gun, because the gap between cathode and anode was smaller and the supporting legs were farther from the cathode. We added an equipotential cylinder between the cathode and the supporting legs to even out the quadrupole effect (Figure 15). We installed the gun back in the test stand and are getting ready to repeat the beam profile measurements.

V. CONCLUSIONS

In conclusion, we have measured the characteristics of a new 1-inch electron gun. We have covered two major characteristics, namely the cathode yield as a function of cathode-anode voltage and as a function of cathode temperature, and beam profile. The perveance measurement illustrated the relation between cathode yield current and cathode-anode voltage. The cathode yield as a function of temperature helped us determine the gun working point: 1100 °C, corresponding to a filament current of 8.75 A. Perveance was measured at this working temperature. The measurements taken in early 2012 and June 2012 show consistent results. The analysis on generalized perveance show that relativistic effects are not dominant, and the neutralization fraction reached a peak of 20.6% at 70 V. The Longo model fitting illustrated the relation between cathode

yield current and cathode temperature. We used all data taken at various temperatures and cathode-anode voltages, including both space-charge limited and temperature limited regimes. The fitting results show effective parameters that characterize the electron gun in a reasonable way.

The beam profile measurements taken in early 2012 and June 2012 consistently show an imperfect concentricity of the cathode in relation with the electrodes. We identified a cathode off-center problem and the electron gun has been disassembled and improved. In addition, we identified a quadrupole effect from the beam profile measurements. We suspected it to be the impact of the supporting legs connected to the anode. We installed a conductive cylinder between the cathode and the legs. We plan to repeat the characterization measurement to check the improved electron gun geometry.

VI. ACKNOWLEDGMENTS

I would like to thank Giulio Stancari for his help and guidance throughout my work on this project, Alexander Valishev and Alexander Didenko for their assistance. I would also like to thank Eric Prebys and Linda Spentzouris for organizing this internship.

APPENDIX A: ORGANIZATION OF WORKING DIRECTORY

My working directory is lisiqi@mrbutts.fnal.gov. The home directory consists of the following subdirectories: /ana for analysis, /report for report, and /data for data. The analysis directory contains all the R scripts to produce the fitting results and plots presented in this paper. Produced plots are saved in the nested directory /plots under /ana. "longo8.R" fits our measurements with Longo's model and produces Figure 12 and the histograms (Figures 11 and 13). "plotItemp.R" plots cathode yield current as a function of temperature at 5000 V (the voltage is tunable in the script) and produces Figure 10 bottom right. "longo7.R" produces Figures 10 top right and bottom left. "heating.R" produces Figure 10 top left. "profile.R" produces 1D and 2D scan of the beam profile. "shapefactor.R" compares the effect of different values of shape factor α, producing Figure 3. "Iop_temp.R" plots cathode yield current as a function of temperature, marked by different colors for different voltages. The report directory contains all drafts that composes this paper, including the original tex files and compiled pdf files. A subdirectory /template nested under the /report directory contains all the formatting information for composing this report. The data directory contains all measurements data related to this paper, including measurements taken from January, February and June 2012. Figures that illustrate the physical appearance of experimental apparatus, including gun geometry diagram, are also saved in the data directory. There is an /old_version directory nested under data and analysis directory, which saves obsolete data, plots and R scripts.

[1] G. Stancari, Phys. Rev. Lett. **107**, 084802 (2011).

[2] G. Stancari et al., Proc. 2011 Part. Accel. Conf. (PAC11), New York, NY, USA, pp. 370–372; G. Stancari et al., Proc. 2011 Int. Part. Accel. Conf. (IPAC11), San Sebastian, Spain, pp. 1939–1941; G. Stancari et al., Proc. 2012 Int. Part. Accel. Conf. (IPAC10), Kyoto, Japan, pp. 1698–1700.

[3] A. S. Gilmour, Jr., in *Principles of Traveling Wave Tubes,* Norwood, MA, 1994, pp. 53.

[4] G. Stancari, Proc. APS/DPF-2011 Conf., Providence, Rhode Island, arXiv:1110.0144, FERMILAB-CONF-11-506-AD-APC.

[5] R. T. Longo, "Physics of Thermionic Dispenser Cathode Aging," Journal of Applied Physics, Volume 94, Number 10, pp. 6966–6975.

[6] R. Vaughan, IEEE Trans. Electron Devices **ED-33**, 11, 1986.

[7] A. Ivanov and M. Tiunov, Proc. 2002 Euro. Part. Accel. Conf. (EPAC02), Paris, France, pp.1634.

[8] M. Reiser, in *Theory and Design of Charged Particle Beams,* Wiley, New York, 1994, pp. 196–197.